Journal Pre-proof

Synthesis and characterization of ceramic high entropy carbide thin films from the Cr-Hf-Mo-Ta-W refractory metal system

T. Stasiak, S. Debnárová, S. Lin, N. Koutná, Zs. Czigány, K. Balázsi, V. Buršíková, P. Vašina, P. Souček

Please cite this article as: T. Stasiak, S. Debnárová, S. Lin et al., Synthesis and characterization of ceramic high entropy carbide thin films from the Cr-Hf-Mo-Ta-W refractory metal system, *Surface & Coatings Technology* (2024), doi: https://doi.org/10.1016/j.surfcoat.2024.130839.

This is a PDF file of an article that has undergone enhancements after acceptance, such as the addition of a cover page and metadata, and formatting for readability, but it is not yet the definitive version of record. This version will undergo additional copyediting, typesetting and review before it is published in its final form, but we are providing this version to give early visibility of the article. Please note that, during the production process, errors may be discovered which could affect the content, and all legal disclaimers that apply to the journal pertain.

Highlights (for review)

Research highlights

- Hybrid PVD-PECVD magnetron sputtering used to prepare high entropy carbides
- HEAs without carbon were bcc, HECs with high enough carbon content were fcc
- Direct bcc-fcc transition predicted; transition via amorphization observed
- High tolerance of C vacancies for the HEC structure
- Best mechanical properties in the amorphous-fcc transition region

Graphical Abstract
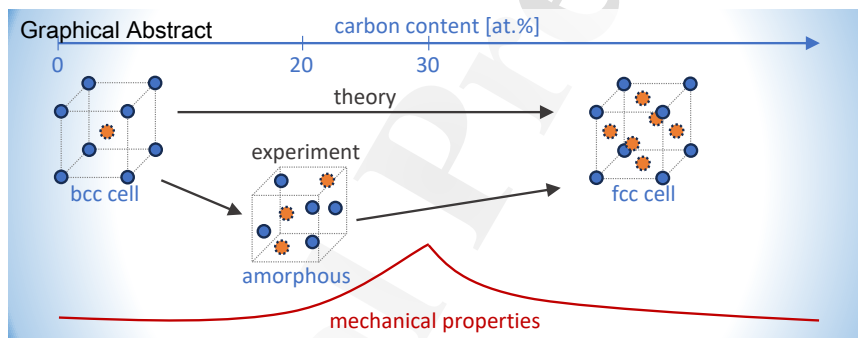
Revised manuscript file

Synthesis and characterization of ceramic high entropy carbide thin films

from the Cr-Hf-Mo-Ta-W refractory metal system

T. Stasiak[1,2], S. Debnárová[1], S. Lin[3,4], N. Koutná[3,4], Zs. Czigány[5], K. Balázsi[5], V. Buršíková[1],

P.Vašina[1], P. Souček[1]*

[1]Department of Plasma Physics and Technology, Masaryk University, Kotlářská 2, CZ-61137

Brno, Czech Republic

[2]National Centre for Nuclear Research, A. Soltana 7, PL-05-400 Otwock-Swierk, Poland

[3]Technische Universität Wien, Institute of Materials Science and Technology, Vienna, A-1060,

Austria

[4]Linköping University, Department of Physics, Chemistry, and Biology (IFM), Linköping,

SE-58183, Sweden

[5]Institute of Technical Physics and Materials Science, HUN-REN Centre for Energy Research,

Konkoly Thege M. út 29-33, Budapest H-1121, Hungary

* Corresponding author: P. Souček, email: soucek@physics.muni.cz, telephone: +420 549 49

8769

1

Abstract

We use reactive DC magnetron sputtering to showcase synthesis strategies for multicomponent carbides with the NaCl-type fcc structure and illustrate how deposition conditions allow controlling the formation of metallic and ceramic single phases in the Cr-Hf-Mo-Ta-W system. The synthesis is performed in argon flow and different acetylene flows from 0 to 12 sccm, at ambient and elevated temperatures (700°C), respectively, hindering/promoting the adatom diffusion. Structural and microstructural investigations reveal the formation of the bcc metallic phase ($a = 3.188 - 3.209$ Å) in films deposited without acetylene flow, also supported by *ab initio* density function theory (DFT) analysis of lattice parameters as a function of the C content. Experimentally, a bcc-to-fcc phase transition is observed through the formation of an amorphous coating. Contrarily, samples deposited in higher acetylene flow show an fcc multielement carbide phase ($a = 4.33 - 4.49$Å). The crystalline films reveal columnar morphology, while the amorphous ones are very dense. We report promising mechanical properties, with hardness up to 25 ± 1 GPa. The indentation moduli reach up to 319 ± 6 GPa and show trends consistent with DFT predictions. Our study paves the path towards the preparation of Cr-Hf-Mo-Ta-W multicomponent carbides by magnetron sputtering, showing promising microstructure as well as mechanical properties.

Keywords: high entropy carbide, high entropy alloy, multicomponent ceramics, multicomponent material, thin film, magnetron sputtering

2

1   Introduction

High-entropy alloys (HEAs), also known as compositionally-complex alloys (CCAs), are multicomponent materials containing at least five main elements with content between 5 and 35 at.% [1]. HEAs can include various elements—such as 3d transition metals, refractory metals, light metals, etc. [2]—and offer a large tunability in physical properties, thus, advantages over traditional single-principal-element alloys. Typically reported properties of HEAs are high strength and hardness at low and high temperatures, outstanding structural stability, good wear resistance, exceptional corrosion and oxidation resistance, good resistance to hydrogen embrittlement, and excellent irradiation resistance [1, 3, 4]. These properties have been commonly attributed to four core effects: high entropy effect (solid solution stabilization), sluggish diffusion (nanocrystalline structure and high thermal stability), lattice distortion (high hardness), and cocktail effect [5].

The concept of high-entropy materials has also been extended to ceramics (precisely referred to as multicomponent or high entropy metal sublattice ceramics), including carbides, nitrides, oxides, and borides, which have been synthesized in bulk as well as thin film form [6]. Magnetron sputtering (MS) deposition of high-entropy thin film ceramics offers great flexibility via adjustment of the deposition conditions, allowing the control of the chemical composition and the microstructure. Among widely researched high-entropy ceramics are oxides and nitrides, illustrating that high-entropy effects provide a good basis for achieving desired property combinations, possibly outperforming binary systems [7]. Though relatively less studied, several high-entropy carbides (HEC) systems have been synthesised [8–19] and have shown promising characteristics, such as high hardness, good creep and oxidation resistance, small thermal conductivity, and biocompatibility [20].

HEC thin films have been deposited from alloyed or elemental targets of different metallic elements [7], where carbon has been introduced via reactive gas, such as methane (CH_4) [8, 9, 12–15], acetylene (C_2H_2) [16–18], or eventually from a solid graphite target [10, 11, 19]. The films most often exhibited the fcc rock-salt structure (NaCl-type). One of the first magnetron-sputtered multielement carbides has been developed by Braic et al. [8], who deposited with argon and methane flow, achieved nearly equimolar compositions at the metallic sublattice (Ti-Al-Cr-Nb-Y), and reported good wear resistance in combination with hardness of 23.5 GPa. Through variations of the carbon content, the films were shown to exhibit either single-phase fcc structure (carbon content close to stoichiometry) or an amorphous structure (carbon contents of ≈ 80

3

at. %). Similar observations—including the tendency to form an fcc structure at C contents close to 50 at.% and good wear resistance—were reported also for other HECs [9, 11, 12, 15, 16, 18, 21].

In our previous experimental work, we have demonstrated the possibility of preparing DC magnetron sputtered thin films of the Cr-Hf-Mo-Ta-W family with bcc metallic or fcc nitride single phase [22, 23]. Due to their expected properties, high entropy alloys and ceramics based on refractory elements have great potential in different applications, such as protective coatings for machining at high speeds and temperatures or high-temperature protective coatings in aerospace. In this study, we employ hybrid physical vapour deposition - plasma enhanced chemical vapour deposition (PVD-PECVD) non-saturated magnetron sputtering from segmented targets under argon and acetylene flow to showcase this synthesis strategy for the same combination of metallic elements combined with carbon. The main aim is to establish the relationship between the structure, microstructure, mechanical proprieties, and deposition parameters such as acetylene flow and temperature.

4

2 Materials and methods

2.1 Synthesis

Thin films from the Cr-Hf-Mo-Ta-W system were deposited by reactive DC magnetron sputtering from the elemental targets under acetylene flow. Circular (thickness 3 mm, diameter 50.8 mm) elemental high-purity targets (Cr 99.95%, Mo 99.95%, Ta 99.90%, W 99.95% , Hf 99.9%) were purchased from Testbourne Ltd. The targets were cut into four equal segments using a water jet cutter and put into the deposition device – an HVM Flexilab (HVM Plasma spol. s.r.o., Czech Republic). The device is equipped with three magnetron heads in a confocal configuration. The segments in the deposition device were placed in the same configuration as in our previous paper on this multicomponent system [23] and shown schematically in Fig. 1, i.e., cathode 1: four segments of chromium, cathode 2: two segments of molybdenum and two segments of hafnium, cathode 3: two segments of tantalum and two segments of tungsten. The power of the cathodes was set, based on the sputtering yield of pure elements [24], as cathode 1 = 80 W, cathode 2 = 150 W, and cathode 3 = 150 W to obtain near equimolar composition after deposition without acetylene flow. The depositions were performed on a silicon (100) wafer of 2 x 1 cm in size. The substrate was ultrasonically cleaned in acetone and then in isopropanol for 180 seconds before placement in the centre of the substrate holder. The base pressure before the deposition was approximately 2×10^{-4} Pa, obtained using two pumps - an oil-free scroll vacuum pump (Anest Iwata, Japan) and a turbopump Hipace 300 (Pfeiffer, Germany). The substrate was also cleaned for 15 minutes directly before the deposition by argon ions under the pressure of 2.00 Pa using a 13.56 MHz generated DC self-bias of –180 V to remove any contamination and oxidation. Subsequently, the targets, which were separated by shutters from the substrate, were cleaned by argon ions at 1.26 Pa for 15 minutes using the same power of cathodes as for deposition. Each deposition was performed for 30 minutes. The rotation of the substrate was set to 5 rotations per minute (rpm). The distance between each target and the substrate was 110 mm. The argon flow was fixed at 80 standard cubic centimetres per minute (sccm) for all depositions. It resulted in a pressure of 1.26 Pa for depositions without acetylene (C_2H_2) flow. The reactive magnetron sputtering depositions were carried out, besides constant argon flow, at acetylene flow of 1 sccm (corresponding to a total pressure of 1.27 Pa), 2 sccm (1.27 Pa), 2.5 sccm (1.27 Pa), 3 sccm (1.28 Pa), 4.5 sccm (1.29 Pa), 6 sccm (1.30 Pa), 7 sccm (1.31 Pa), 8 sccm (1.32 Pa), 9 sccm (1.32 Pa) and 12 sccm (1.35 Pa). The samples were deposited at ambient room temperature (abbreviated by RT; without intentional heating, < 50°C) and at high temperature

5

(abbreviated by HT; 700°C). For HT samples, the temperature was steadily raised to 700°C and then maintained for 1 h for stabilising before the deposition.
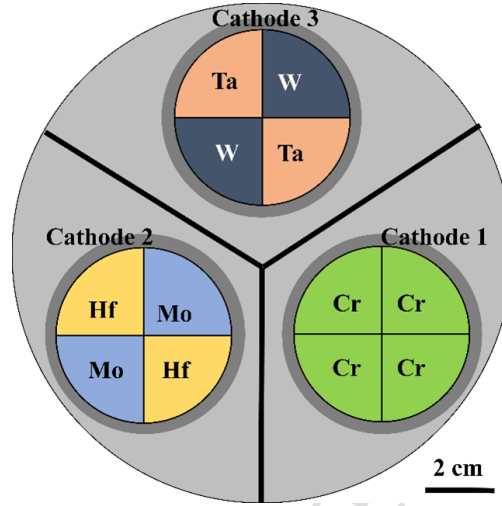

Figure 1: Configuration of targets on three cathodes.

2.2 Characterization

Scanning electron microscopy (SEM) observations of the top view and cross-section of deposited coatings were performed with a TESCAN MIRA 3 SEM (TESCAN, Czech Republic) working at 15 kV accelerating voltage. The microscope was equipped with an energy-dispersive X-ray spectroscopy (EDX) detector (X-MAX[50], Oxford Instruments, UK) for the chemical composition measurements, which were done based on two 275 x 235 μm EDX maps. The quantification was done using factory standards provided in the AZtec library. The deposition rate was calculated based on multiple cross-section images from different parts of the samples. The X-ray diffraction (XRD) investigations were carried out using a Rigaku SmartLab diffractometer with a copper $K\alpha$ radiation source ($\lambda = 1.54056$ Å). The XRD data examination was conducted using the Rigaku PDXL software and the ICDD database. The crystallite size in bcc metallic and fcc carbide thin films was calculated using the Halder-Wagner method [25]. The mechanical properties investigations were carried out using a Hysitron 950 TriboIndenter equipped with XPM. The indentations were conducted under a maximum force of 2 mN and 5 mN. For each force, 100 indentations were performed. The data obtained with these two forces did not differ above experimental errors. The measured indentation data were analyzed using Oliver and Pharr [26] method to determine hardness (H) and effective Young's modulus (E_{eff}). The FIB lamellae

6

for TEM investigations were made using a Thermo Scientific Scios 2 Dual Beam microscope. The final steps in FIB preparation were made at 2kV. The TEM investigations themselves were performed in a C_s corrected 200kV Themis microscope by Thermo Fischer Scientific. The SAED patterns were evaluated by the Process Diffraction software [27].

2.3   Ab initio and molecular dynamics calculations

Ab initio calculations were carried out based on the projector augmented wave (PAW) method using the Vienna *Ab initio* Simulation Package (VASP) [28,29]. The exchange-correlation functional was approximated using the Perdew-Burke-Ernzerhof functional revised for solids (PBEsol) [30], with a plane-wave cutoff energy of 600 eV. Our computational model for fcc-based (Fm$\bar{3}$m) (Cr,Hf,Mo,Ta,W)C was based on a $3 \times 3 \times 3$ replica (108 metal + 108 C atoms) of the conventional fcc cell. Transition metals were distributed on the metallic sublattice according to the special quasi-random structures (SQS) method [31,32], in approximately equimolar distribution. Additionally, we generated 8 variants of this supercell containing (disordered) C vacancies, (Cr,Hf,Mo,Ta,W)C$_x$, where $x = \{0, 0.286, 0.50, 0.667, 0.751, 0.826, 0.887, 0.946, 1.0\}$. Again, the vacancies were distributed according to the above-mentioned SQS method [33–36]. Setting a k-mesh sampling of the Brillouin zone to $4 \times 4 \times 4$, all structures were fully optimized (in terms of atomic positions, cell shape, and volume) until forces on all atoms were below 10^{-5} eV/Å.

Chemical stability was estimated by calculating the energy of formation, E_f,

$$E_f = \frac{1}{\sum_s n_s} \left(E_{\text{tot}} - \sum_s n_s \mu_s \right) , \qquad (1)$$

where E_{tot} is the total energy of the simulation cell (corresponding to the last ionic step in a VASP relaxation), n_s and μ_s are the number of atoms and the chemical potential, respectively, of a species s. Chemical potentials μ_s, of the element $s =$ were conventionally set to the total energy per atom of the ground-state structure of the respective element (according to Material's project [37]), that is hcp-Hf and bcc-Ta, -Cr, -Mo, -W, and graphite-C.

To estimate room-temperature mechanical properties of selected (Cr,Hf,Mo,Ta,W)C$_x$ systems, Born-Oppenheimer *ab initio* molecular dynamics (AIMD) calculations were carried out, again with the aid of the VASP package [28,29], the same exchange-correlation functional as in the above zero Kelvin calculations but only a Γ-point sampling of the Brillouin zone. To find equilibrium lattice parameters at 300 K, we run a 4 ps simulation with the isobaric-isothermal (NPT) ensemble (using Parrinello-Rahman barostat [38] and Langevin thermostat). Subsequently, we

7

run a 2 ps simulations with the canonical (NVT) ensemble (using Nosé-Hoover thermostat) with time-averaged lattice parameters from the NPT simulation. Subsequently, we applied series of deformations—[001] tensile and (001)[100] shear—in order to evaluate elastic constants, C_{ij}. Both the tensile and shear simulations were performed for strains of each with a 2% and 4% and methodologically followed Refs. [39–41]. Elastic constants were extracted from a second-order polynomial fit of the tress/strain data (following Ref. [42]), assuming strains up to 4%. Elastic properties, such as the polycrystalline Young's modulus, $E = 9BG/(3B + G)$ were calculated using the Hill's average of the bulk, B, and shear modulus, G [43, 44]

8

3 Results and discussion

3.1 Deposition rate and chemical composition

For both room- and high-temperature series of samples, denoted by RT and HT in Fig. 2, the deposition rate is high and ranges from ~ 40 nm/min to ~ 65 nm/min. For RT series, the deposition rate first increases with increasing the acetylene flow, reaching the maximum of 64 nm/min at 4.5 sccm of acetylene. We suggest that this may be interpreted by increasingly easier carbon incorporation in the lattice and a higher gas flow, thus higher pressure and increased sputter yield of targets. However, at acetylene flow above 4.5 sccm, a carbon-rich layer forming on the targets causes target poisoning, subsequently reducing the sputtering rate [8, 13, 21]. HT series show similar trends but lower deposition rates than the RT case, which could be due to higher densification of thin films at HT [45] or increased desorption of atoms of some elements adsorbed on the substrate [7].
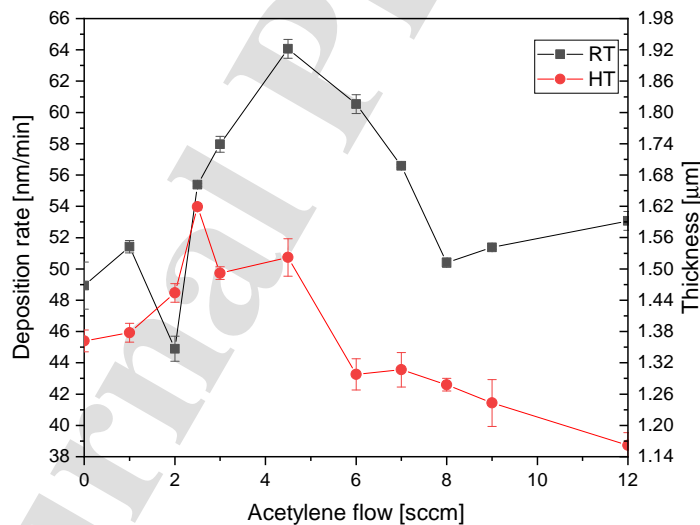

Figure 2: The deposition rate and thickness of samples prepared at RT and HT as a function of acetylene flow.

Also, in terms of chemical composition (determined by EDX measurements, with error bar of ± 2 at.%) both room- and high-temperature deposition conditions result in similar trends, see Fig. 3. The samples show low oxygen contamination ($2-3$ at.%, not depicted in Fig. 3), common for

9

deposition processes similar to ours. Contrarily to the same Cr-Hf-Mo-Ta-W system sputtered in nitrogen [23], the chemical composition exhibits a nearly linear increase of carbon content with increasing acetylene flow for both series of samples without any sign of saturation. Above 6 sccm of acetylene flow, the carbon content clearly exceeds the ideal stoichiometric case, indicating a non-saturated reactive process (also called a hybrid PVD-PECVD process) commonly observed in reactively sputtered carbides [46,47]. The phenomenon has been explained by the hybrid nature of the sputtering process for carbides, where excess carbon is incorporated into the coating as a pure carbon [46,47]. The content of metallic elements in films deposited without acetylene flow is $18-22$ at.% for the RT series and $15-22$ at.% for the HT series. The content of metallic elements decreases with increasing the carbon content, the most significantly for Cr (~ 0 at.% at 9 sccm of C_2H_2). The power of the cathode containing Cr was the lowest (80 W) among the cathodes. It could favour the creation of the carbon layer on the targets and, therefore, significantly reduce the sputtering rate.
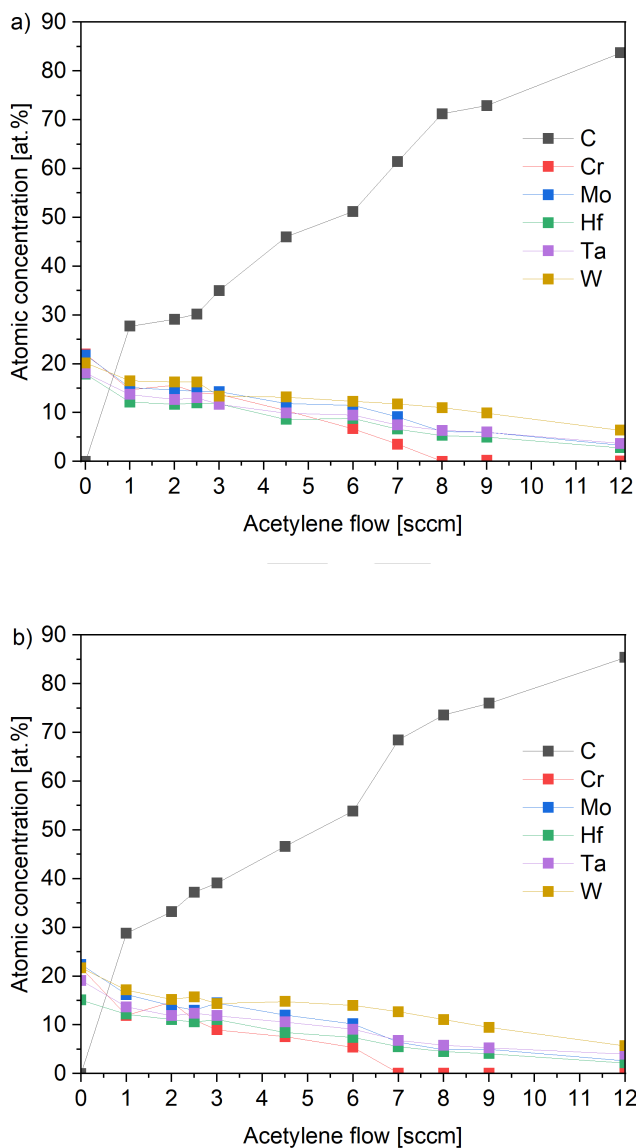
10

Figure 3: Chemical composition of films deposited at RT (a) and HT (b) at different flows of acetylene.

11

3.2 Morphology and Microstructure

The SEM observations of the top view and cross-section (Fig. 4) reveal differences in the films' microstructure and morphology. The samples deposited at 0 sccm of acetylene at RT and HT exhibit columnar microstructure, common for many metallic HEA thin films [48–51]. For the HT sample, the surface morphology exhibits much sharper facets often connected to enhanced crystallisation of the sample. The films deposited at 2 sccm of acetylene present a dense microstructure without any apparent columnar structure or voids in the volume of the film. There are no significant differences between RT and HT series. The samples deposited at acetylene flow between 3 and 9 sccm of acetylene flow again exhibit columnar structure, except the film prepared at 9 sccm of acetylene at RT, which presents a denser microstructure. The columnar microstructure is frequently observed in multicomponent carbides deposited by magnetron sputtering [9, 11, 12, 17]. The columns are more pronounced in the HT series of samples.

3.3 Crystalline structure

The XRD investigations (Fig. 5) reveal different crystalline structures depending on the deposition conditions. Samples deposited without acetylene flow show a metallic bcc phase, expectable since is favoured by most of the constituting metals (Cr, Mo, Ta, W) where only Hf crystallizes in a hexagonal phase. Furthermore, the formation of the bcc-CrHfMoTaW has also been predicted by theoretical studies [52, 53]. The measured lattice parameters—(3.209 ± 0.006) Å and (3.188 ± 0.011) Å for the RT and HT samples, respectively—are close to those the rule of mixture for components with bcc phases ($a_{\mathrm{Cr}} = 2.91$ Å, $a_{\mathrm{Mo}} = 3.15$ Å, $a_{\mathrm{Ta}} = 3.30$ Å, $a_{\mathrm{W}} = 3.17$ Å [37]). The small difference in RT and HT lattice parameters could be ascribed to differences in their chemical composition (Fig. 3). Furthermore, small satellite peaks observed near the (110) peak may reflect the formation of bcc phases with a slightly different chemical composition stemming from the rotation of the substrate holder, as shown in TEM results (supplementary S1) and was also observed in our earlier work [23]. The sample deposited at 1 sccm C_2H_2 flow at RT exhibits an X-ray amorphous structure, while the sample deposited at HT exhibits the bcc structure, although with a smaller crystallite size compared to 0 sccm. The sample deposited at 2 sccm C_2H_2 flow at RT reveals an X-ray amorphous structure. This may be due to the carbon content being too low to form a crystalline fcc phase but too high to retain a bcc metallic phase. In contrast, the sample deposited at HT shows a nanocrystalline structure with most probably fcc peaks considerably shifted between the pure fcc and bcc positions. Similar observations for elements
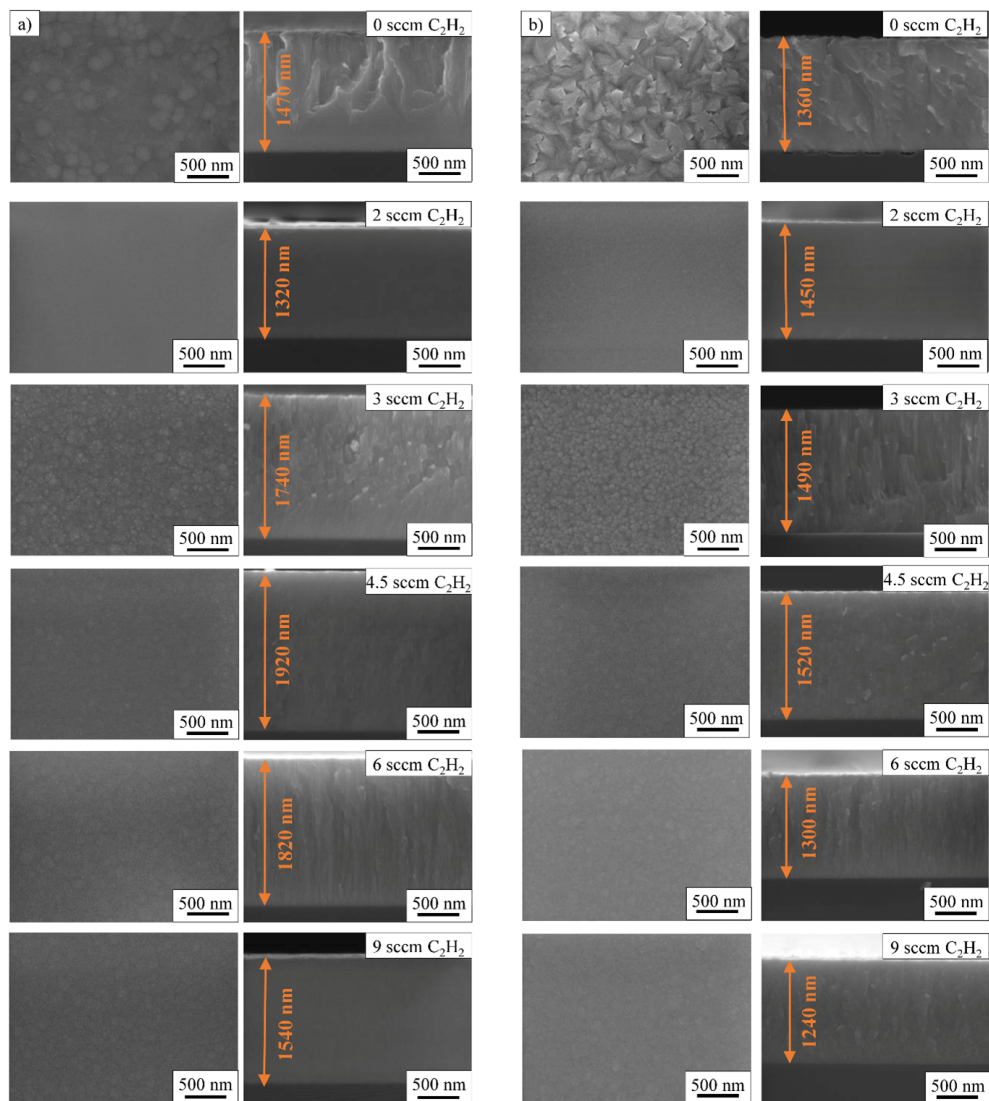
12

Figure 4: SEM results of samples deposited at RT (a) and HT (b) at different acetylene flows. Left-side images show the top view, while right-side images show the cross-section.

introduced via a gas phase were reported in our previous study [23] (the same metal elements, Cr-Hf-Mo-Ta-W, but deposition at nitrogen flow) and by others [17] (TaNbSiZrCrC, deposited at acetylene flow).

The X-ray amorphous structure of samples deposited at $2\,\mathrm{sccm}$ C_2H_2 is in agreement with SEM results (Fig. 4), showing a dense microstructure and smooth surface, common for the amorphous structure [8]. The samples deposited between 3 and $7\,\mathrm{sccm}$ of acetylene show the fcc carbide phase, thus demonstrating the ability of the Cr-Hf-Mo-Ta-W family to form multielement fcc carbide. Note that four of the constituent elements form binary carbides of an fcc structure (HfC [54], TaC [55], MoC [56], WC [57]) and one exists in multiple competing phases (fcc-$Cr_{23}C_6$, orthorhombic-Cr_7C_3 and Cr_3C_2 [58]). The sample deposited at $9\,\mathrm{sccm}$ of acetylene and RT exhibits an X-ray amorphous or short-range ordered structure, which agrees with other studies on multicomponent carbides [17,21]. In contrast, the corresponding sample deposited at HT reveals an fcc single carbide phase. Here, again, the temperature of the substrate during deposition has an important effect by favouring the formation of fcc carbide instead of the X-ray amorphous phase.

The sample deposited at $3\,\mathrm{sccm}$ of acetylene flow at HT reveals a strong texture with the dominant peak of the (111) plane. The preferred orientation of (111) was reported in other studies of multielement carbides [8,9,11,12,14,15]. In the fcc NaCl-type structure, the (111) plane presents the lowest strain energy, while the (200) shows the lowest surface energy. Therefore, there is competition between planes during the film growth. The preferred orientation usually depends on the conditions of the magnetron sputtering process and the film thickness. As magnetron-sputtered films generally have high intrinsic stress and strain energy, the preferential orientation should be the one with the lowest strain energy, i.e. (111), to lower the overall energy of the film [59]. Similar to our previous observation for Cr-Hf-Mo-Ta-W nitride [23], XRD-derived lattice parameters of Cr-Hf-Mo-Ta-W carbide (Fig. 6) increase with increasing the carbon content, presumably as C fills vacancies at the non-metal sublattice until reaching stoichiometry ($\sim 50\,\mathrm{at.\%}$ of C). For higher carbon contents (C over-stoichiometric films), C may start filling interstitial sites.

The crystallite size measurements (Fig. 7) show only small differences between HT at RT conditions and confirm the nanocrystalline size of crystallites in all films. The bcc HEAs exhibit the largest crystallite size (~ 15–$20\,\mathrm{nm}$), while the size of the fcc grains is smaller except for the film prepared at HT at 3 sccm of acetylene. The crystallite size in the fcc systems generally
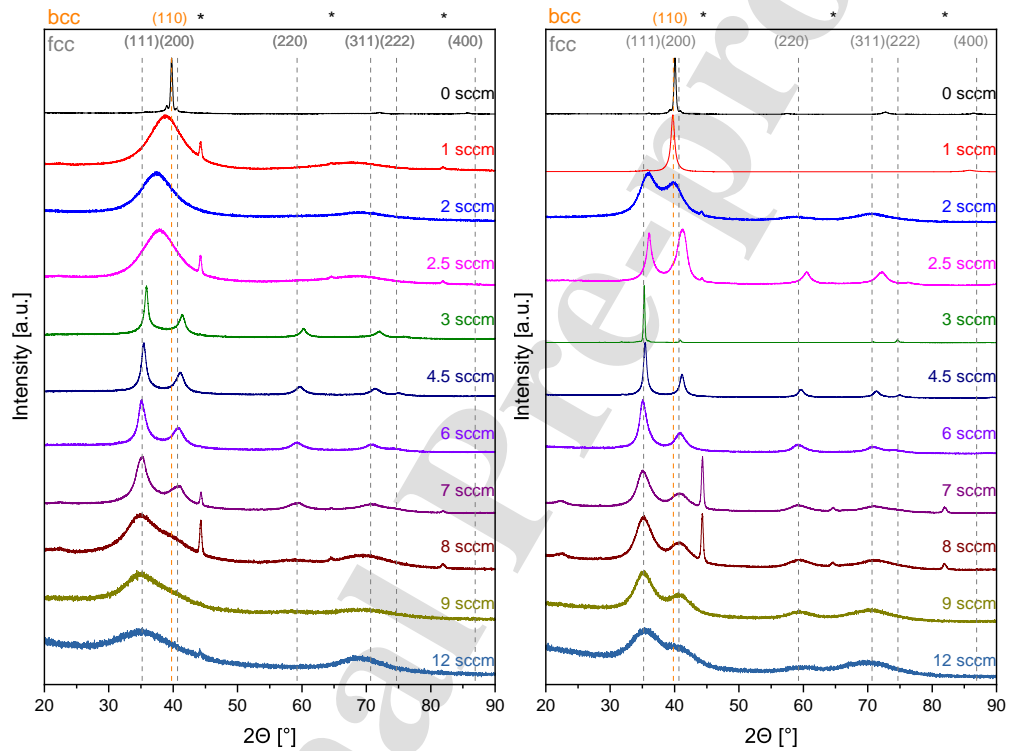
14

Figure 5: X-ray diffractograms of samples deposited at RT (a) and HT (b) at different acetylene flows. Positions of relevant peaks with their miller indices are shown at the top of the image. Fcc diffractions are shown in grey and bcc in orange. Sample holder (steel) peak positions are denoted by asterisks.
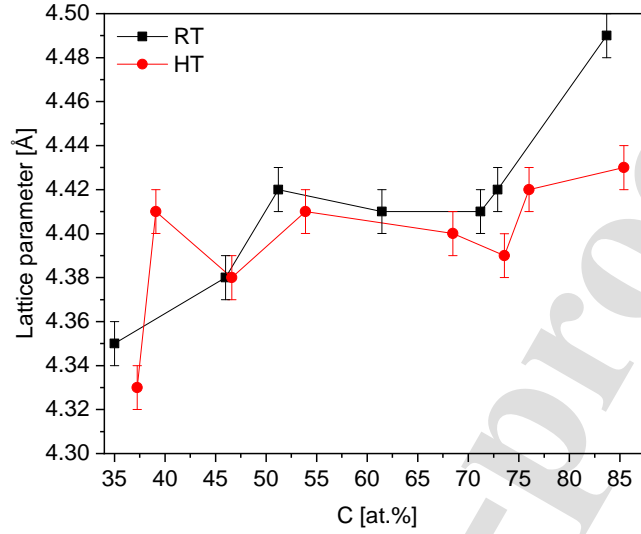
15

Figure 6: The lattice parameter of samples with the fcc carbide phase prepared at RT and HT as a function of the carbon content.

decreases with increasing acetylene flow. Our values are comparable with those reported for other magnetron-sputtered multicomponent carbide thin films [9, 12, 14, 15, 18]. The crystallite size of the fcc carbides is smaller (again, except the sample deposited at $3\,\mathrm{sccm}$ C_2H_2 at HT with ~ 42 at.% of C) than fcc nitrides from the same multicomponent system [23]. Braic et al. [15] also found that carbide films present smaller crystallite sizes than nitride films for the Ti-Zr-Nb-Hf-Ta system.

To support experimental observations on structural evolution in relationship with the C content, *ab inito* density functional theory (DFT) calculations have been carried out. Fig. 8(a) depicts formation energies, E_f (calculated following Eq. 1), indicating relative chemical stability of (Cr,Hf,Mo,Ta,W)C_x systems. Specifically, the C content, x, ranges from 0 (corresponding to bcc-(Cr,Hf,Mo,Ta,W)) to 1 (corresponding to fcc (Cr,Hf,Mo,Ta,W)C, i.e., with 50at.% of C and all non-metallic lattice sites fully occupied). Starting from (Cr,Hf,Mo,Ta,W)C ($x = 1$, $E_f \approx -0.15$ eV/at.) and generating C vacancies (decreasing x), E_f decreases, hence, indicating increased chemical stability of the system. The lowest E_f (≈ -0.19 eV/at.) is obtained for $x \approx 0.83$, which corresponds to $\approx 20\%$ of vacancies on the C sublattice. From this point, further C content decrease induces an E_f increase, turning to positive values—thus, becoming energetically unstable—at $x \approx 0.29$. Structural analysis of the corresponding supercells in terms of lattice
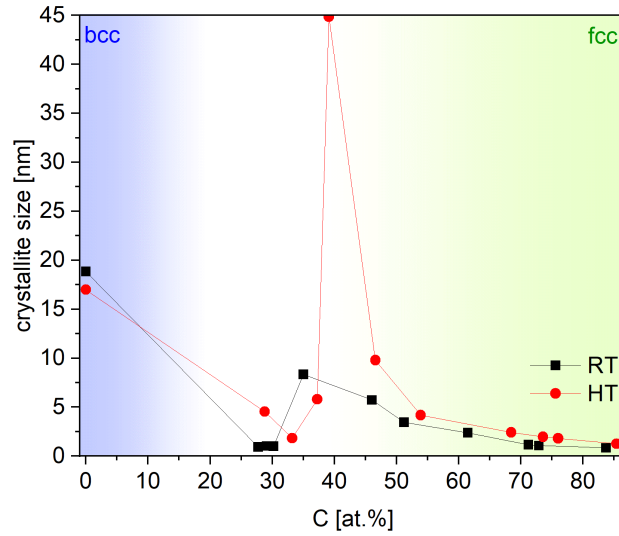
16

Figure 7: The crystallite size of samples prepared at RT and HT as a function of the carbon content.

parameters (Fig. 8b) shows a linear decrease upon decreasing the C content (for numerical details of the fit, see the shaded box in Fig. 8b). Note that relaxation of our initially perfectly cubic supercells leads to three generally different lattice parameters ($a \neq b \neq c$) as a consequence of lattice distortions through (i) the high-entropy metal sublattice and (b) partially occupied C sublattice. In Fig. 8b, we depict the average cubic lattice parameter together with the standard deviation, indicating how much the underlying structure deviates from the cubic symmetry. While for $x = 1$ and $x = 0$, i.e. the ideal fcc and bcc structures, these deviations are nearly zero (stemming only from the high-entropy effect of the metal sublattice), some compositions in-between exhibit significantly non-cubic symmetry. Therefore, the formation of the fcc lattice will be hindered. Specifically, the non-cubic compositions are those yielding $x \lesssim 0.5$, which correspond to structures with relatively high or even positive formation energies. In summary, (Cr, Hf, Mo, Ta, W)C$_x$ thin films with low C contents of ~ 25 at.% will no longer crystallise in the fcc cell, as was observed experimentally in our work. This tetragonal distortion is the first step in the Bain scheme of the fcc–bct–bcc transition used to describe the martensitic transformation in steels [60]. In high entropy (or multicomponent) materials, the tetragonal fcc–bcc transition was experimentally observed in Hf-Nb-Ti-V-Zr nitride coatings through the broadening of certain XRD peaks, while others did not change [61]. In our case, this direct observation is not possible due to small crystallites and texture. The columns and especially the inter-columnar walls of the

17

sample prepared at 3 sccm at high temperature exhibited increased content of oxygen, probably showing increased porosity of the crystalline fcc coatings with columnar structure.
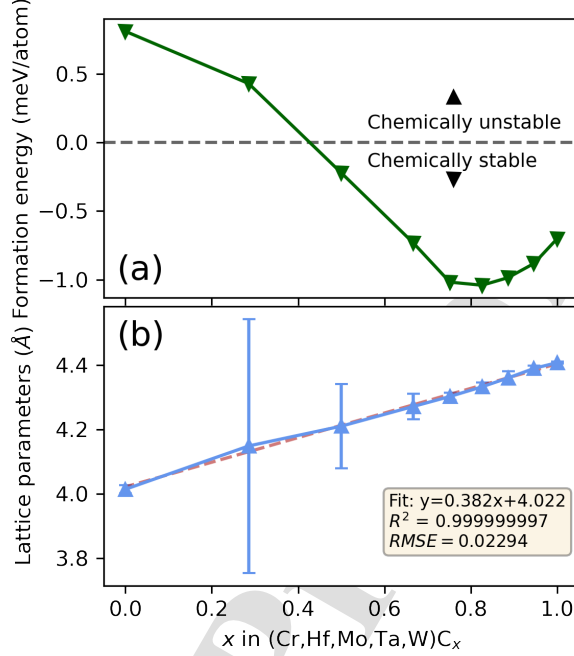

Figure 8: (a) Calculated formation energy, E_f, as a function of the C content, x, in $(\mathrm{Cr,Hf,Mo,Ta,W})\mathrm{C}_x$. Negative (positive) E_f values indicate chemical stability (instability). (b) The corresponding cubic lattice parameters—calculated by averaging lengths of the a, b, and c lattice vectors—together with a linear fit (numerical details in the shaded frame). The error bars are standard deviations, indicating deviations from perfect cubic symmetry.

Samples at the transition region from both the ambient room temperature (RT) and HT series prepared at the acetylene flows of 2.5 and 3 sccm, corresponding to carbon contents $\sim$ 30–40 at.% were further investigated by transmission electron microscopy (TEM). High-resolution TEM images are shown in Figure 9. Low-magnification images are shown in the supplementary materials in Figure S1. All coatings reveal the expected multilayered character and a compositional modulation due to sample holder rotation under the different targets, as the geometry is not ideally confocal [23]. The sample prepared at RT and 2.5 sccm—containing $\sim$ 30 at.% of C and being X-ray amorphous (recall Fig. 5)—was shown amorphous also by HRTEM and the SAED pattern analysis. Furthermore, we observe a trace of a columnar structure with $\sim$ 20 nm wide columns in the growth direction spanning the whole sample thickness. As the acetylene flow is increased to 3 sccm and the carbon content to $\sim$ 35 at.% of C, the coating exhibits a compet-

18

itive growth with V-shaped features (typically on 20 nm scale width), resulting in ~ 7 nm wide grains. There are amorphous walls between the V-shape columns, and the detected grains are fcc (with the d-spacing of 4.41 Å). Thus, the bcc-to-fcc transition in a low-energy (diffusion-limiting) environment does not occur simply through tetragonal distortions but requires an intermediate step, amorphisation. For the HT series, both samples exhibit fcc structure. The d-spacing for the samples prepared at 2.5 sccm (~ 37 at.% C) and 3 sccm of acetylene (~ 39 at.% of C) were 4.38 Å and 4.41 Å, respectively. The coating prepared at 2.5 sccm again exhibited competitive growth with ~ 20 nm wide V-shaped features with elongated grains ~ 7 nm wide and ~ 50 nm high. The walls between the V-shape features were again amorphous. As the acetylene flow was increased to 3 sccm, the coating's structure changed to a clear columnar structure. The columns mostly spanned through the film thickness. The lateral grain size was limited by the column width to ~ 20 nm, and the vertical size was up to the coating thickness. This explains the very sharp peak observed on the XRD (recall Fig. 5). For the high-temperature series, the bcc-fcc transition was probably shifted to the acetylene flows around 2 sccm due to higher carbon content at the same acetylene flow for the HT series.

Additionally, the sample prepared at the highest acetylene flow of 12 sccm at high temperature was imaged by TEM. This sample contains ~ 85 at.% of carbon (see Fig. 3) and a hint of very broad fcc reflections in the X-ray diffractograms (see Fig. 5). The sample has no columnar structure and is homogeneous in this regard. It exhibits compositional variation and multilayer structure, such as all the rest of the films (see Fig. S6 in the Supplementary material). HR image shown in Fig. 10a reveals that the film is predominantly nanocrystalline with ~ 1 nm crystallite size. The SAED pattern from an area with a diameter of ~ 600 nm reproduced in Fig. 10b shows very broad rings that can be identified as originating from an fcc structure with a lattice parameter of 4.41Å. No significant fraction of any purely amorphous phase was observed even though the sample contained ~ 85 at.% of carbon. The high amount of excess carbon could be, therefore, only in a very thin tissue phase on the crystallite boundaries or in metal element vacancies in the crystallites as is theoretically predicted for simple single-phase fcc carbides [62,63].

3.4   Mechanical Properties

Fig. 11a depicts the hardness of our coatings as a function of the carbon content. Specifically, metallic films deposited at 0 sccm acetylene flow show similar hardness ($11 - 11.8$ GPa) at the RT
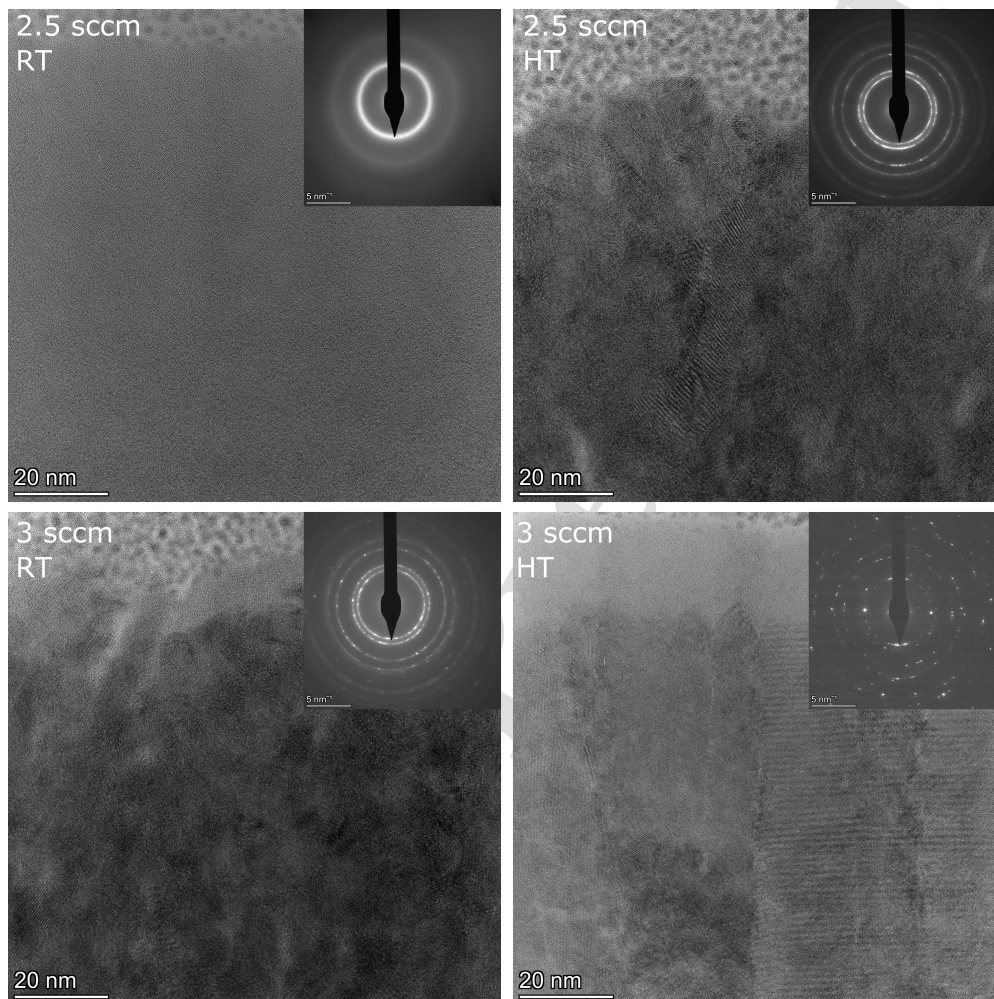
19

Figure 9: High-resolution TEM images of samples prepared at 2.5 sccm and 3 sccm of acetylene at ambient room temperature (RT) and high temperature (HT). The SAED patterns are shown as insets of the images of the corresponding coatings. The sample prepared at 2.5sscm at RT sample is amorphous, while all the others are polycrystalline with a fcc crystal structure. The nanocrystalline region visible over the film is the Pt-C protection layer deposited for FIB sample preparation. Individual full-size images are shown in the supplementary material as Figs. S2 – S4.
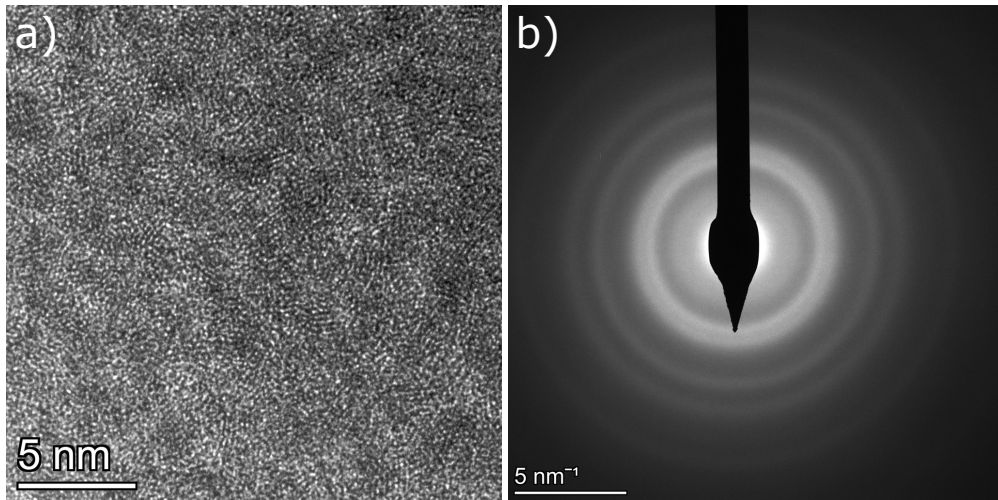
Figure 10: a) High-resolution TEM image of the sample prepared at 12 sccm at high temperature (HT). b) Corresponding SAED pattern. The sample is predominantly polycrystalline with a fcc crystal structure and the lattice parameter of 4.41 Å.

and HT conditions. For comparison, other magnetron-sputtered HEAs typically exhibit slightly lower values, e.g. 8.7 GPa for the AlCrFeMnMo film [51] or 9.7 GPa for the CrNbTiMoZr [64]. Our higher hardness may be due to using only refractory metals, most of which form hard bcc binary compounds themselves. Films deposited at 2 sccm acetylene flow at RT and HT containing ~ 32 at.% of C exhibit the highest hardness among the investigated samples, likely contributed to by their dense structure.

While the sample prepared at RT is amorphous, the sample deposited at HT reveals very broad peaks (small crystallites) corresponding to the fcc carbide structure. The combination of nanocrystallites and the dense structure led to the hardness of (25.0 ± 1.0) GPa, which is the highest among tested samples. The hardness of samples consisting of multielement fcc carbides reaches 16.9–19.0 GPa. For HT samples, the hardness drops to roughly 12 GPa when the carbon content in the coating exceeds 65 at.%. The difference in the crystallite size between carbide samples (Fig. 7) seems not to play an important role in hardness via the Hall-Petch effect [65,66]. The hardness of multicomponent fcc carbide is intermediate, likely influenced by the porosity of our films. For comparison, consider e.g., 32.9 GPa for the (CrNbSiTiZr)C film [16], 34.3 GPa for the (HfNbTiVZr)C film [67]), and, at the lower end, e.g., 17.4 GPa for the (CrNbTiMoZr)C film [18]). In our case, the hardness seems to be mainly limited by very small grains, mostly < 10 nm, favouring the occurrence of the inverse Hall-Petch effect [68].
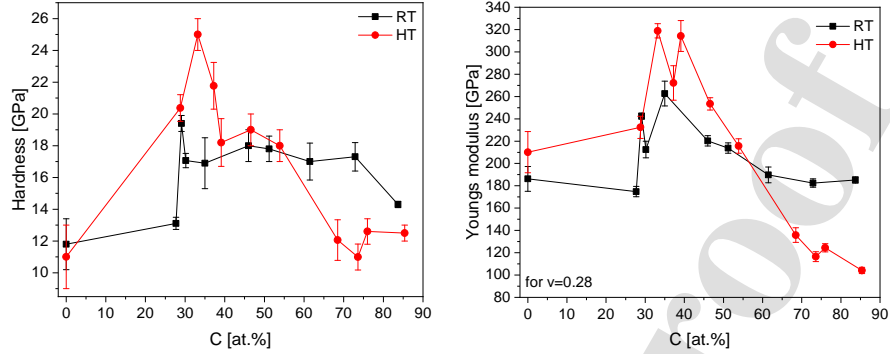
21

Figure 11: Mechanical properties of thin films with different C contents. Hardness is on the left, and Young's modulus is on the right.

Fig. 11b. shows the effective Young's modulus determined from indentation tests as a function of the carbon content. Metallic bcc samples exhibit Young's modulus $180-210\,\text{GPa}$. Samples deposited at $2\,\text{sccm}$ acetylene flow (amorphous/nanocrystalline) and $3\,\text{sccm}$ acetylene flow (fcc multielement carbide) reveal the highest Young's modulus. For these two conditions, Young's modulus is higher for the HT series ($\sim 310\,\text{GPa}$). It could be related to the denser morphology of these films. Above $3\,\text{sccm}$ acetylene flow, Young's modulus decreases with increasing acetylene flow. The decrease in the HT series is more pronounced, probably due to macro- and microstructural evolution.

The hardness (H) to effective Young's modulus (E_{eff}) ratios, H/E_{eff} and H^3/E_{eff}^2 (Fig 12), have been commonly used in the thin film community as wear resistance estimates [69, 70], conveying the relation between plastic flow and mechanical resistance. The formulas approximate the interaction of a high elastic strain to the capability of failure. Clearly, the formulas should not be over-interpreted, as they disregard e.g. fracture toughness [71]. In this study, both parameters show a rather similar trend as a function of acetylene flow. The metallic bcc films present relatively low H/E_{eff} and H^3/E_{eff}^2 values, comparable to that of the amorphous CrNbSiTiZr film ($H/E \approx 0.053$, $H^3/E^2 \approx 0.028$ [48]), or the AlCrFeMnMo film ($H/E \approx 0.048$, $H^3/E^2 \approx 0.020$ [51]). For samples deposited at $2\,\text{sccm}$ acetylene flow, presenting amorphous (RT) and amorphous/nanocrystalline structure (HT), both parameters significantly increase compared to the metallic samples. Films prepared at $3\,\text{sccm}$ acetylene flow show lower H/E_{eff} and H^3/E_{eff}^2 ratios, possibly due to their less dense columnar microstructure. However, both ratios increase with increasing the acetylene flow due to a decrease in the effective Young's modulus. Our

22

values are comparable with other multicomponent carbide thin films, e.g., (CrNbTiMoZr)C with $H/E \approx 0.08$ and $H^3/E^2 \approx 0.12$ [18], (CrNbTaTiW)C films with $H/E \approx 0.043$–0.088 [11], or TaNbSiZrCr carbides with $H/E \approx 0.051$–0.082 and $H^3/E^2 \approx 0.077$–0.132.
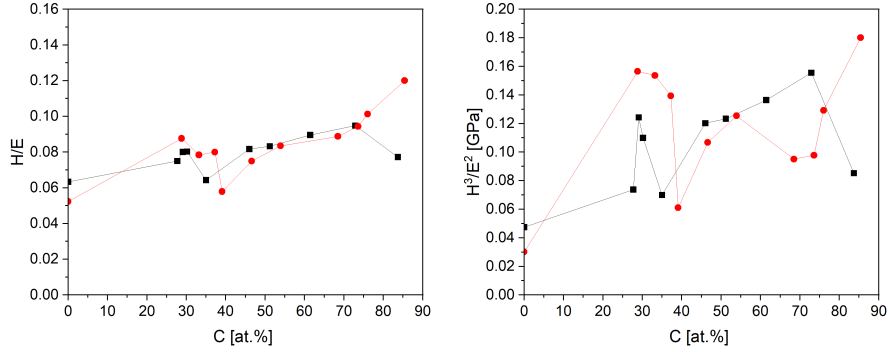

Figure 12: The a) H/E$_{\text{eff}}$ and b) H^3/E$^2_{\text{eff}}$ ratios of thin films with different C contents at RT and HT.

To complement experimental observations, we also simulate room-temperature mechanical response of $(Cr,Hf,Mo,Ta,W)C_x$ using *ab inito* methods, specifically, employing AIMD calculations (for details, see the Methodology section). The predicted elastic constants and the polycrystalline and directional elastic moduli are presented in Tab. 1. Our model always represents an ideal fcc-based single-crystal, where only the content of the C sublattice varies and, following these changes, also lattice parameters are allowed to change (through relaxations of the cell shape, volume, and ionic positions). The calculated $(Cr,Hf,Mo,Ta,W)C_x$ compounds all satisfy conditions for mechanical stability. However, note that bcc-(Cr,Hf,Mo,Ta,W) yields positive formation energy, i.e., is very metastable (assessing its dynamical stability through phonon calculations is out of the scope of the present study). Consistent with the experiment, our results indicate a decrease in the C content from 50 at.% (corresponding to (Cr,Hf,Mo,Ta,W)C) causes a decrease in Young's modulus, E, and also the bulk and shear modulus (B, G). The decrease of E is indeed pronounced: by nearly 50% when going from the fcc-(Cr,Hf,Mo,Ta,W)C ($E \approx 311$ GPa) to bcc-(Cr,Hf,Mo,Ta,W) ($E \approx 155$ GPa). A similar trend is also observed for the directional Young's moduli evaluated along low-index crystallographic directions, [100], [110], and [111], where the [100] directions exhibit the most pronounced drop when more and more vacancies are generated at the C sublattice.

23

In summary, according to *ab inito* dynamics at 300K, $(Cr,Hf,Mo,Ta,W)C_{0.75}$ and $(Cr,Hf,Mo,Ta,W)C$ exhibit similar mechanical properties both being close to the ideal fcc structure. $(Cr,Hf,Mo,Ta,W)C_{0.5}$ has its mechanical properties closer to the bcc-$(Cr,Hf,Mo,Ta,W)C$, which is especially evident in the Poisson's ratio. This indicates more plastic behaviour due to the lack of carbon and the majority of metallic bonds. It seems that $(Cr,Hf,Mo,Ta,W)C_x$ tolerates a high number of C vacancies on the C sublattice without significant change in its mechanical properties. In our case, 25% of vacancies did not affect the elastic properties, and $\gtrsim$ 50% of C vacancies in $(Cr,Hf,Mo,Ta,W)C_{0.5}$ led to elastic properties close to those of the bcc-$(Cr,Hf,Mo,Ta,W)C$.

Although we cannot claim quantitative agreement with the measured indentation moduli due to, e.g. small supercell size and microstructural effects not accounted for in the simulations, AIMD clearly underpins the experimentally observed trends.

Table 1: Room-temperature elastic constants, C_{ij} (in GPa), of $(Cr,Hf,Mo,Ta,W)C_x$ compounds—derived from AIMD calculations (for details see the Methodology section)—together with the polycrystalline bulk modulus, B, polycrystalline shear modulus, G (in GPa), polycrystalline and directional Young's modulus, E (in GPa), and Poisson's ratio, ν.

Compound	C_{11}	C_{44}	C_{12}	E	$E_{[100]}$	$E_{[110]}$	$E_{[111]}$	B	G	ν
fcc-$(Cr,Hf,Mo,Ta,W)C$	397	123	157	311	308	312	314	237	122	0.281
fcc-$(Cr,Hf,Mo,Ta,W)C_{0.75}$	380	115	154	293	291	294	295	229	114	0.286
fcc/bcc-$(Cr,Hf,Mo,Ta,W)C_{0.5}$	286	85	185	188	141	197	227	218	69	0.357
bcc-(Cr,Hf,Mo,Ta,W)	254	58	141	155	153	155	156	179	57	0.355

24

4 Conclusions

Metallic (bcc) and ceramic carbon-based (fcc) Cr-Hf-Mo-Ta-W multicomponent thin films were prepared by magnetron sputtering at room temperature and at 700°C in an argon/acetylene mixture. All deposition conditions resulted in high deposition rates (38–64 nm/min), while the structure and mechanical properties varied as a function of the acetylene flow. Samples deposited without acetylene presented a bcc metallic single phase. At RT and HT depositions, the system formed a bcc phase. The formation of either the fcc or the bcc structure —depending on the C content—was also indicated by DFT calculations. The experimentally-observed bcc-to-fcc transition did occur through amorphisation, likely due to low energies of diffusing atoms. The films deposited at $3-6$ sccm of acetylene flow showed the formation of the fcc carbide, demonstrating the ability of this multielement system to form a single multicomponent carbide phase within the whole range of chosen deposition conditions. Our films presented hardness up to 25 ± 1 GPa and high Young's modulus up to 319 ± 6 GPa, which are high in comparison to other multicomponent thin films. Furthermore, the H/E_{eff} and H^3/E_{eff}^2 ratios suggested high wear resistance of Cr-Hf-Mo-Ta-W multicomponent carbide thin films. In conclusion, our work has shown the possibilities of preparing high entropy carbides by hybrid PVD-PECVD non-saturated magnetron sputtering with segmented targets.

Acknowledgements

25

References

[1] M. C. Gao, P. K. Liaw, J. Wei Yeh, and Y. Zhang. *High-entropy alloys: Fundamentals and applications.* Springer International Publishing, 1 2016.

[2] S. Gorsse, D. B. Miracle, and O. N. Senkov. Mapping the world of complex concentrated alloys. *Acta Mater.*, 135:177–187, 8 2017.

[3] M. Hung Tsai and J. Wei Yeh. High-entropy alloys: A critical review. *Mater. Res. Lett.*, 2:107–123, 2014.

[4] P. A. Ibrahim, I. Ozkul, and C. A. Canbay. An overview of high-entropy alloys. *Emerg. Mater.*, 5:1779–1796, 12 2022.

[5] J. Wei Yeh. Recent progress in high-entropy alloys. *Ann. Chim.-Sci. Mat.*, 31:633–648, 11 2006.

[6] C. Oses, C. Toher, and S. Curtarolo. High-entropy ceramics. *Nature Rev. Mat.*, 5:295–309, 4 2020.

[7] M. El Garah, P. Briois, and F. Sanchette. Recent Progress on High-Entropy Films Deposited by Magnetron Sputtering. *Crystals*, 12, 3 2022.

[8] M. Braic, V. Braic, M. Balaceanu, C. N. Zoita, A. Vladescu, and E. Grigore. Characteristics of (TiAlCrNbY)C films deposited by reactive magnetron sputtering. *Surf. Coat. Technol.*, 204:2010–2014, 3 2010.

[9] V. Braic, A. C. Parau, I. Pana, M. Braic, and M. Balaceanu. Effects of substrate temperature and carbon content on the structure and properties of (CrCuNbTiY)C multicomponent coatings. *Surf. Coat. Technol.*, 258:996–1005, 11 2014.

[10] L. Zendejas Medina, M. V. Tavares da Costa, E. M. Paschalidou, G. Lindwall, L. Riekehr, M. Korvela, S. Fritze, S. Kolozsvǎri, E. K. Gamstedt, L. Nyholm, and U. Jansson. Enhancing corrosion resistance, hardness, and crack resistance in magnetron sputtered high entropy CoCrFeMnNi coatings by adding carbon. *Mater. Design*, 205, 7 2021.

[11] P. Malinovskis, S. Fritze, L. Riekehr, L. von Fieandt, J. Cedervall, D. Rehnlund, L. Nyholm, E. Lewin, and U. Jansson. Synthesis and characterization of multicomponent (CrNbTaTiW)C films for increased hardness and corrosion resistance. *Mater. Design*, 149:51–62, 7 2018.

26

[12] M. Dinu, I. Pana, V. Braic, F. Miculescu, M. Balaceanu, A. Vladescu, and M. Braic. In vitro corrosion resistance of Si containing multi-principal element carbide coatings. *Mater. Corros.*, 67:908–914, 9 2016.

[13] M. Delower Hossain, T. Borman, N. S. McIlwaine, and J. P. Maria. Bipolar high-power impulse magnetron sputtering synthesis of high-entropy carbides. *J. Amer. Ceram. Soc.*, 105:3862–3873, 6 2022.

[14] A. Vladescu, I. Titorencu, Y. Dekhtyar, V. Jinga, V. Pruna, M. Balaceanu, M. Dinu, I. Pana, V. Vendina, and M. Braic. In vitro biocompatibility of Si alloyed multi-principal element carbide coatings. *PLoS ONE*, 11, 8 2016.

[15] V. Braic, M. Balaceanu, M. Braic, A. Vladescu, S. Panseri, and A. Russo. Characterization of multi-principal-element (TiZrNbHfTa)N and (TiZrNbHfTa)C coatings for biomedical applications. *J. Mech. Behav.Biomed.*, 10:197–205, 6 2012.

[16] J. Wang, H. Zhang, X. Yu, L. Wang, W. Huang, and Z. Lu. Insight into the structure and tribological and corrosion performance of high entropy (CrNbSiTiZr)C films: First-principles and experimental study. *Surf. Coat. Technol.*, 421, 9 2021.

[17] W. H. Kao, Y. L. Su, J. H. Horng, and W. C. Wu. Mechanical, tribological, anti-corrosion and anti-glass sticking properties of high-entropy TaNbSiZrCr carbide coatings prepared using radio-frequency magnetron sputtering. *Mater. Chem. Phys.*, 268, 8 2021.

[18] S. Kuang, J. Wang, L. Wang, W. Huang, and Z. Zhou. Improvement of the mechanical and the tribological properties of CrNbTiMoZr coatings through the incorporation of carbon and the adjustment of the substrate bias voltage. *Surf. Coat. Technol.*, 412, 4 2021.

[19] V. Perekrestov, Y. Kosminska, and B. Dyoshyn. Fabrication of Multicomponent Carbide Coatings by Modified Magnetron Sputter Deposition. *Proceedings of the 2019 IEEE 9th International Conference on Nanomaterials: Applications and Properties, NAP 2019*, 9 2019.

[20] S. Akrami, P. Edalati, M. Fuji, and K. Edalati. High-entropy ceramics: Review of principles, production and applications. *Mat. Sci. Eng. R*, 146, 10 2021.

[21] Y. Siang Jhong, C. Wei Huang, and S. Jien Lin. Effects of CH_4 flow ratio on the structure and properties of reactively sputtered $(CrNbSiTiZr)C_x$ coatings. *Mater. Chem. Phys.*, 210:348–352, 5 2018.

27

[22] T. Stasiak, P. Souček, V. Buršíková, and P. Vašina. Magnetron sputtering deposition of high entropy nitrides from chromium-hafnium-molybdenum-tantalum-wolfram system. *NANOCON Conference Proceedings - International Conference on Nanomaterials*, pages 98–103, 2021.

[23] T. Stasiak, P. Souček, V. Buršíková, N. Koutná, Zs. Czigány, K. Balázsi, and P. Vašina. Synthesis and characterization of the ceramic refractory metal high entropy nitride thin films from Cr-Hf-Mo-Ta-W system. *Surf. Coat. Technol.*, 449, 11 2022.

[24] Y. Yamamura and H. Tawara. Energy dependence of ion-induced sputtering yields from monatomic solids at normal incidence. *Atom. Data Nucl. Data*, 62:149–253, 1996.

[25] N. C. Halder and C. N. J. Wagner. Separation of particle size and lattice strain in integral breadth measurements. *Acta Crystallogr.*, 20:312–313, 2 1966.

[26] W.C. Oliver and G.M. Pharr. An improved technique for determining hardness and elastic modulus using load and displacement sensing indentation experiments. *J. Mater. Res.*, 7:1564–1583, 6 1992.

[27] János L Lábár, Miklós Adamik, BP Barna, Zs Czigány, Zs Fogarassy, Zsolt Endre Horváth, Olga Geszti, Fanni Misják, J Morgiel, G Radnóczi, et al. Electron diffraction based analysis of phase fractions and texture in nanocrystalline thin films, part III: Application examples. *Microsc. Microanal.*, 18(2):406–420, 2012.

[28] G. Kresse and J. Furthmüller. Efficient iterative schemes for ab initio total-energy calculations using a plane-wave basis set. *Phys. Rev. B*, 54(16):11169, 1996.

[29] G. Kresse and D. Joubert. From ultrasoft pseudopotentials to the projector augmented-wave method. *Phys. Rev. B*, 59:1758–1775, Jan 1999.

[30] J.P. Perdew, A. Ruzsinszky, G.I. Csonka, O.A. Vydrov, G.E. Scuseria, L.A. Constantin, X. Zhou, and K. Burke. Restoring the density-gradient expansion for exchange in solids and surfaces. *Phys. Rev. Lett.*, 100:136406, Apr 2008.

[31] S-H Wei, LG Ferreira, James E Bernard, and A. Zunger. Electronic properties of random alloys: Special quasirandom structures. *Phys. Rev. B*, 42(15):9622, 1990.

[32] A. Zunger, S-H Wei, L.G. Ferreira, and JE Bernard. Special quasirandom structures. *Phys. Rev. Lett.*, 65(3):353, 1990.

28

[33] L.Y. Tian, G. Wang, J.S. Harris, D.L. Irving, J. Zhao, and L. Vitos. Alloying effect on the elastic properties of refractory high-entropy alloys. *Mater. Design*, 114:243–252, 2017.

[34] C. Jiang and B.P. Uberuaga. Efficient ab initio modeling of random multicomponent alloys. *Phys. rev. lett.*, 116(10):105501, 2016.

[35] M. Dahlqvist, A. Petruhins, J. Lu, L. Hultman, and J. Rosen. Origin of chemically ordered atomic laminates (i-MAX): expanding the elemental space by a theoretical/experimental approach. *ACS nano*, 12(8):7761–7770, 2018.

[36] B. Alling, L. Hultberg, L. Hultman, and I.A. Abrikosov. Strong electron correlations stabilize paramagnetic cubic $Cr_{1-x}Al_xN$ solid solutions. *Appl. Phys. Lett.*, 102(3), 2013.

[37] A. Jain, S.P. Ong, G. Hautier, W. Chen, W.D. Richards, S. Dacek, S. Cholia, D. Gunter, D. Skinner, G. Ceder, et al. Commentary: The Materials Project: A materials genome approach to accelerating materials innovation. *APL Mater.*, 1(1):011002, 2013.

[38] M. Parrinello and A. Rahman. Polymorphic transitions in single crystals: A new molecular dynamics method. *J. Appl. Phys.*, 52(12):7182–7190, 1981.

[39] D. G. Sangiovanni, F. Tasnadi, L. J. S. Johnson, M. Odén, and I. A. Abrikosov. Strength, transformation toughening, and fracture dynamics of rocksalt-structure $Ti_{1-x}Al_xN$ ($0 \leq x \leq 0.75$) alloys. *Phys. Rev. Mat.*, 4(3):033605, 2020.

[40] D. G. Sangiovanni. Inherent toughness and fracture mechanisms of refractory transition-metal nitrides via density-functional molecular dynamics. *Acta Mater.*, 151:11–20, 2018.

[41] A. B. Mei, H. Kindlund, E. Broitman, L. Hultman, I. Petrov, J. E. Greene, and D. G. Sangiovanni. Adaptive hard and tough mechanical response in single-crystal B1 VN_x ceramics via control of anion vacancies. *Acta Mater.*, 192:78–88, 2020.

[42] D. G. Sangiovanni, F. Tasnadi, T. Harrington, M. Odén, K. S. Vecchio, and I. A. Abrikosov. Temperature-dependent elastic properties of binary and multicomponent high-entropy refractory carbides. *Mater. Design*, 204:109634, 2021.

[43] J. F. Nye. *Physical properties of crystals: their representation by tensors and matrices.* Oxford university press, 1985.

[44] R. Hill. The elastic behaviour of a crystalline aggregate. *Proc. Phys. Soc. A*, 65(5):349, 1952.

[45] S. Chang Liang, Z. Chin Chang, D. Cheng Tsai, Y. Chen Lin, H. Shin Sung, M. Jen Deng, and F. Sheng Shieu. Effects of substrate temperature on the structure and mechanical properties of (TiVCrZrHf)N coatings. *Appl. Surf. Sci.*, 257:7709–7713, 6 2011.

[46] T. Schmidtová, P. Souček, V. Kudrle, and P. Vašina. Non-monotonous evolution of hybrid PVD–PECVD process characteristics on hydrocarbon supply. *Surf. Coat. Technol.*, 232:283–289, 2013.

[47] T. Nyberg, H. Högberg, G. Greczynski, and S. Berg. A simple model for non-saturated reactive sputtering processes. *Thin Solid Films*, 688, 2019.

[48] X. Yu, J. Wang, L. Wang, and W. Huang. Fabrication and characterization of CrNbSiTiZr high-entropy alloy films by radio-frequency magnetron sputtering via tuning substrate bias. *Surf. Coat. Technol.*, 412, 4 2021.

[49] Hanuel Kim, Seungjin Nam, Aeran Roh, Myungwoo Son, Moon Ho Ham, Jae Hun Kim, and Hyunjoo Choi. Mechanical and electrical properties of NbMoTaW refractory high-entropy alloy thin films. *Int. J. Refract. Met. H.*, 80:286–291, 4 2019.

[50] X. Sun, X. Cheng, H. Cai, S. Ma, Z. Xu, and T. Ali. Microstructure, mechanical and physical properties of feconialmnw high-entropy films deposited by magnetron sputtering. *Appl. Surf. Sci.*, 507, 3 2020.

[51] Y. Y. Santana, M. A. Sow, C. Nouvellon, C. Cordier, F. Beclin, M. Touzin, A. Tromont, X. Noirfalise, L. Boilet, J. F. Trelcat, M. Dubar, H. Morvan, and M. Bigerelle. Influence of powder mixing method on properties of high entropy alloys of FeCrMnAlMo thin coatings obtained by magnetron sputtering. *Surf. Coat. Technol.*, 446, 9 2022.

[52] Y. Lederer, C. Toher, K. S. Vecchio, and S. Curtarolo. The search for high entropy alloys: A high-throughput ab-initio approach. *Acta Mater.*, 159:364–383, 10 2018.

[53] K. Kaufmann and K. S. Vecchio. Searching for high entropy alloys: A machine learning approach. *Acta Mater.*, 198:178–222, 10 2020.

[54] K. Hans, S. Latha, P. Bera, and Harish C. Barshilia. Hafnium carbide based solar absorber coatings with high spectral selectivity. *Sol. Energ. Mat. Sol. C.*, 185:1–7, 10 2018.

[55] M. Vargas, H. A. Castillo, E. Restrepo-Parra, and W. De La Cruz. Stoichiometry behavior of TaN, TaCN and TaC thin films produced by magnetron sputtering. *Appl. Surf. Sci.*, 279:7–12, 8 2013.

[56] D. Dinesh Kumar, N. Kumar, Kalpatru Panda, A. M. Kamalan Kirubaharan, and P. Kup-
pusami. Tribochemistry of contact interfaces of nanocrystalline molybdenum carbide films.
Appl. Surf. Sci., 447:677–686, 7 2018.

[57] L. C. Agudelo-Morimitsu, J. De La Roche, D. Escobar, R. Ospina, and E. Restrepo-Parra.
Substrate heating and post-annealing effect on tungsten/tungsten carbide bilayers grown by
non-reactive DC magnetron sputtering. *Ceram. Int.*, 39:7355–7365, 9 2013.

[58] C. Ziebert, J. Ye, M. Stueber, S. Ulrich, M. Edinger, and I. Barzen. Ion bombardment-
induced nanocrystallization of magnetron-sputtered chromium carbide thin films. *Surf.
Coat. Technol.*, 205:4844–4849, 7 2011.

[59] U. C. Oh and J.H. Je. Effects of strain energy on the preferred orientation of TiN thin films.
J. Appl. Phys., 74:1692–1696, 1993.

[60] C. Cayron. One-step model of the face-centred-cubic to body-centred-cubic martensitic
transformation. *Acta Crystallogr. A*, 69(5):498–509, 2013.

[61] K. Johansson, L. Riekehr, S. Fritze, and E. Lewin. Multicomponent Hf-Nb-Ti-V-Zr nitride
coatings by reactive magnetron sputter deposition. *Surf. Coat. Technol.*, 349:529–539, 2018.

[62] X. Tang, R. Salehin, G.B. Thompson, and C.R. Weinberger. Statistical study of vacancy
diffusion in TiC and TaC. *Phys. Rev. Mater.*, 4(9), September 2020.

[63] E. Smirnova, M. Nourazar, and P.A. Korzhavyi. Internal structure of metal vacancies in
cubic carbides. *Phys. Rev. B*, 109(6), February 2024.

[64] J. Wang, S. Kuang, X. Yu, L. Wang, and W. Huang. Tribo-mechanical properties of CrNbTi-
MoZr high-entropy alloy film synthesized by direct current magnetron sputtering. *Surf. Coat.
Technol.*, 403, 12 2020.

[65] EO Hall. The deformation and ageing of mild steel: III discussion of results. *Proc. Phys.
Soc. B*, 64(9):747, 1951.

[66] NJ Petch. The cleavage strength of polycrystals. *J. Iron Steel Inst.*, 174:25–28, 1953.

[67] B. Osinger, H. Mao, S. Fritze, L. Riekehr, U. Jansson, and E. Lewin. Investigation of
the phase formation in magnetron sputtered hard multicomponent (HfNbTiVZr)C coatings.
Mater. Design, 221, 9 2022.

31

[68] CE Carlton and PJ Ferreira. What is behind the inverse Hall–Petch effect in nanocrystalline materials? *Acta Mater.*, 55(11):3749–3756, 2007.

[69] A. Leyland and A. Matthews. On the significance of the H/E ratio in wear control: A nanocomposite coating approach to optimised tribological behaviour. *Wear*, 246:1–11, 11 2000.

[70] P. H. Mayrhofer, C. Mitterer, and J. Musil. Structure-property relationships in single- and dual-phase nanocrystalline hard coatings. *Surf. Coat. Technol.*, 174-175:725–731, 2003.

[71] X. Chen, Y. Du, and Y. Wah Chung. Commentary on using H/E and H^3/E^2 as proxies for fracture toughness of hard coatings. *Thin Solid Films*, 688, 10 2019.

Declaration of interests

☒ The authors declare that they have no known competing financial interests or personal relationships that could have appeared to influence the work reported in this paper.

☐ The author is an Editorial Board Member/Editor-in-Chief/Associate Editor/Guest Editor for [Journal name] and was not involved in the editorial review or the decision to publish this article.

☐ The authors declare the following financial interests/personal relationships which may be considered as potential competing interests: